MATERIALS SCIENCE

Single-atom nanozymes

Liang Huang[1,2], Jinxing Chen[1,2], Linfeng Gan[1,3], Jin Wang[4]*, Shaojun Dong[1,2]*

Conventional nanozyme technologies face formidable challenges of intricate size-, composition-, and facet-dependent catalysis and inherently low active site density. We discovered a new class of single-atom nanozymes with atomically dispersed enzyme-like active sites in nanomaterials, which significantly enhanced catalytic performance, and uncovered the underlying mechanism. With oxidase catalysis as a model reaction, experimental studies and theoretical calculations revealed that single-atom nanozymes with carbon nanoframe–confined FeN_5 active centers (FeN_5 SA/CNF) catalytically behaved like the axial ligand–coordinated heme of cytochrome P450. The definite active moieties and crucial synergistic effects endow FeN_5 SA/CNF with a clear electron push-effect mechanism, as well as the highest oxidase-like activity among other nanozymes (the rate constant is 70 times higher than that of commercial Pt/C) and versatile antibacterial applications. These suggest that the single-atom nanozymes have great potential to become the next-generation nanozymes.

INTRODUCTION

Nanozymes, catalytic nanomaterials with enzyme-like characteristics (*1*, *2*), have attracted enormous research interests in recent years for the unique advantages of low cost, high stability, tunable catalytic activity, and ease of mass production, as well as storage, which endow them with wide applications in biosensing, tissue engineering, therapeutics, and environmental protection (*3*, *4*). Since Yan and coworkers (*5*) discovered the unexpected peroxidase mimicking activity of magnetic iron oxide nanoparticles, various nanozymes have been achieved by nanomaterials, such as metal oxides, noble metals, carbon materials, and metal-organic frameworks (MOFs) (*6*–*16*). However, there remain two contemporary challenges facing nanozyme technologies. First, the enzyme-like activity is the most decisive factor for replacing natural enzymes, but nanozymes with low densities of active sites always show much lower catalytic activity than natural enzymes (*17*, *18*). Second, the inhomogenous elemental composition and facet structure exposed by diverse nanozymes result in different and complicated catalytic mechanisms (*19*, *20*), which make it extremely difficult to distinguish the actual active sites and search for the origin of enzyme-like activity. Thus, these bottlenecks seriously restrict the extensive applications of conventional nanozymes.

To resolve these issues, we discovered a new class of single-atom nanozymes, which integrated the state-of-the-art single-atom technology with intrinsic enzyme-like active sites. The atomically dispersed metal centers maximized the atomic utilization efficiency and density of active sites. Meanwhile, the well-defined coordination structure provided a clear experimental model for mechanism investigation. Single-atom nanozymes have universal significance, because the catalytic activity and mechanism depend mainly on the steric configuration of active centers, rather than the size, structure, or facet of the supported nanomaterials. Hence, the enzyme-like properties of a certain type of active site could be used for potential applications with altering morphology of the supports. In addition, it is feasible to integrate the diverse enzyme-like activities and catalytic mechanisms of different single-atom nanozymes by investigating the countable kinds of single-atom active centers.

In this study, we report an effective and general method for the synthesis of highly active single-atom nanozymes through mimicking the spatial structure of enzymic active centers. The single-atom nanozymes of carbon nanoframe–confined axial N-coordinated single-atom Fe (FeN_5 SA/CNF) were prepared through a bottom-up strategy. The active sites of FeN_5 SA/CNF resembled the axial ligand–coordinated heme of natural redox enzymes (fig. S1). With oxidase catalysis as a model reaction, theoretical calculations and experimental studies unambiguously identified that the highest oxidase-like activity of FeN_5 SA/CNF was derived from the crucial synergistic effect and electron donation mechanism. Notably, FeN_5 SA/CNF exhibited 17 and 70 times higher oxidase-like activity than that of square planar FeN_4 catalyst and commercial Pt/C with normalized metal content, respectively. This indicates the unexpected oxidase-like push effect of axial N coordination in FeN_5 SA/CNF, and its significantly enhanced catalytic activity compared to conventional nanozymes. It boosts the mechanistic understanding of single-atom nanozymes.

RESULTS

Synthesis and characterization of FeN_5 SA/CNF

For the synthesis of FeN_5 SA/CNF, we first designed a host-guest structure of MOF-encapsulated iron phthalocyanine (FePc) (FePc@Zn-MOF) and then pyrolyzed the precursor at 900°C under N_2 atmosphere to obtain single-atom nanozymes. Our previous work has demonstrated that the square planar FeN_4 sites would be retained during the calcination of iron porphyrin and FePc, but the monodispersed sites tend to agglomerate into nanoparticles in the absence of substrate support (*21*–*29*). During the carbonization process, secondary building units of nitrogenous organic linkers transformed into pyridinic N carbon nanoframes and Zn ions were evaporated. Meanwhile, the isolated FeN_4 sites within the confinement of carbon nanoframes were reconstructed and coordinated with the pyridinic N substrate to generate more thermodynamic stable FeN_5/C sites (Fig. 1A).

[1]State Key Laboratory of Electroanalytical Chemistry, Changchun Institute of Applied Chemistry, Chinese Academy of Sciences, Changchun, Jilin 130022, China. [2]University of Science and Technology of China, Hefei, Anhui 230026, China. [3]University of Chinese Academy of Sciences, Beijing 100049, China. [4]Department of Chemistry and Physics, Stony Brook University, Stony Brook, NY 11794-3400, USA.
*Corresponding author. Email: jin.d.wang@gmail.com (J.W.); dongsj@ciac.ac.cn (S.D.)

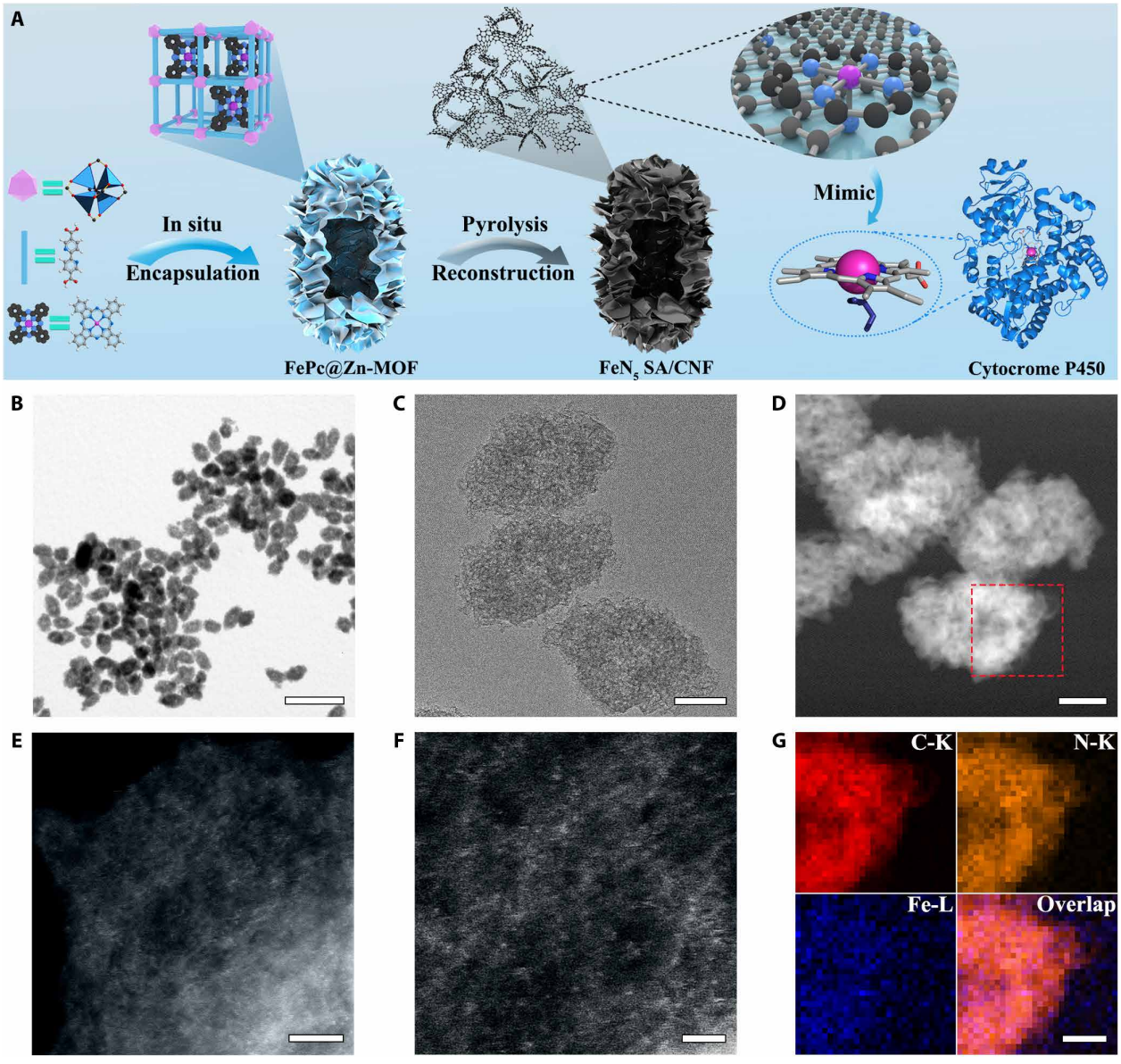

Fig. 1. Synthetic scheme and morphology characterization of FeN_5SA/CNF. (**A**) Schematic formation process of carbon nanoframe–confined atomically dispersed Fe sites with axial five-N coordination for mimicking the active center of cytocrome P450. (**B** and **C**) TEM images and (**D**) high-angle annular dark-field STEM (HAADF-STEM) image of FeN_5 SA/CNF. (**E** and **F**) Magnified HAADF-STEM images of FeN_5 SA/CNF showing the dominant metal single atom. (**G**) EELS mapping images of FeN_5 SA/CNF of the selected region in (D). Scale bars, 1 μm and 100, 100, 5, 2, and 50 nm (B to G, respectively).

The morphology and structure of FeN_5 SA/CNF were characterized with a number of techniques. Representative scanning electron microscopy (SEM) and transmission electron microscopy (TEM) images reveal that the fusiform FePc@Zn-MOF is the dominant product with uniform morphology (fig. S2). The average length and diameter of the precursor are 400 and 200 nm, respectively. The hollow cavities and porous shells endow FePc@Zn-MOF with high specific surface areas and abundant hierarchical nanopores (fig. S3B). The x-ray diffraction (XRD) patterns indicate that the crystal structure of Zn-MOF undergoes no significant change after in situ encapsulating FePc (fig. S3A). The Fourier transform infrared (FTIR) spectrum of FePc@Zn-MOF indicates the successful encapsulation of FePc (fig. S4). FeN_5 SA/CNF obtained from pyrolysis of FePc@Zn-MOF precursor at 900°C has maintained its original morphology and porous property (Fig. 1, B to D, and fig. S5, A to C). The Brunauer-Emmett-Teller surface area of FeN_5 SA/CNF reaches 1407 $m^2 g^{-1}$, and the average pore diameters are 0.8 and 3.4 nm (figs. S5D and S6). The high-resolution TEM (HRTEM) images, selected-area electron diffraction, and XRD patterns exhibit no observable particles or characteristic crystal peaks, excluding the formation of nanoparticles (figs. S5E and S7A). Furthermore, atomic-resolution scanning TEM (STEM) *Z*-contrast images of FeN_5 SA/CNF confirm the existence of atomically dispersed Fe atoms over the carbon nanosheets, and the observation of multiple regions indicates that only individual Fe atoms are present in FeN_5 SA/CNF (Fig. 1, E and F, and fig. S7B). The electron energy-loss spectroscopy (EELS) mapping images show

that the Fe and N atoms are homogeneously distributed throughout the whole domain, indicating the generation of Fe–N sites in three-dimensional matrices (Fig. 1G and fig. S5F). We used inductively coupled plasma–mass spectrometry (ICP-MS) and elementary analysis to identify the loadings of Fe [1.2 weight % (wt %)] and N (4.8 wt %) elements, respectively.

Atomic structure analysis of FeN_5 SA/CNF

We used x-ray photoelectron spectroscopy (XPS), x-ray absorption fine structure (XAFS), and Mössbauer spectroscopy to further characterize the atomic structures of FeN_5 SA/CNF. The XPS Fe 2p spectrum shows two peaks at binding energies of 711.2 eV (Fe $2p^{3/2}$) and 724.5 eV (Fe $2p^{1/2}$). The XPS N 1s spectrum can be principally deconvoluted into pyridinic N, which, derived from organic linkers, could serve as attachment sites for coupling the FeN_4 active centers (Fig. 2A and fig. S8, A to C). The Fe K-edge x-ray absorption near-edge structure (XANES) of FeN_5 SA/CNF, with Fe foil, Fe_2O_3, and FePc as references, is shown in Fig. 2B. The pre-edge peak at 7117 eV that appears in the samples is similar to FePc, suggesting that the FeN_5 SA/CNF samples contain a similar FeN_4 structure (*24*, *29*). Moreover, Fourier-transformed k^3-weighted extended XAFS (FT-EXAFS) spectrum of FeN_5 SA/CNF at Fe K-edge presents a main peak at 1.55 Å, which is in accord with Fe–N scattering path, and no Fe—O bond (1.50 Å) or Fe—Fe bond (2.13 Å) is detected, indicating the formation of atomically dispersed Fe–N sites in FeN_5 SA/CNF (Fig. 2C). The corresponding EXAFS fitting of the first coordination shell was performed to determine the structural parameters and quantitative chemical configuration of Fe atoms (Fig. 2D). The coordination number of Fe atom is nearly five, which indicates the formation of Fe–N_5 moieties in FeN_5 SA/CNF. We used Mössbauer spectroscopy to investigate the electron structure and Fe coordination of FeN_5 SA/CNF based on the recoil-free absorption of γ rays by Fe^{57} nuclei (fig. S8D). The Mössbauer spectrum is deconvoluted into three different doublets according to the isomer shift (δ_{iso}) and quadrupole splitting (ΔE_Q) values (table S1). The distinctive quadrupole doublet of the second doublet with the smallest δ_{iso} value of 0.13 mm s^{-1} and the largest ΔE_Q value of 2.75 mm s^{-1} can be assigned to a N-$Fe^{III}N_4$ medium-spin species with five coordinated rhombic monopyramidal structures (*25*, *29*, *30*). The relative absorption area (24.65%) of that second doublet indicates the high content of FeN_5 moieties in FeN_5 SA/CNF.

Oxidase-like activity assays

We determined the oxidase-like activities of FeN_5 SA/CNF by colorimetric assays. We used the oxidation of 3,3′,5,5′-tetramethylbenzidine (TMB) as a model catalytic reaction to investigate the interaction of O_2 molecules with FeN_5 SA/CNF in various environments (Fig. 3A). We prepared a series of referenced catalysts through this general method with simply altering the pyrolytic temperature, organic ligand, and metal phthalocyanine (MPc) of the MPc@Zn-MOF precursor (figs. S9 to S15). The HRTEM and high-angle annular dark-field STEM (HAADF-STEM) images exhibit no observable particles, excluding the formation of nanoparticles in these catalysts. Furthermore, FT-EXAFS spectra of MN_x SA/CNF at the K-edge present a main peak corresponding to the M–N scattering path, and metal bond is detected, indicating the formation of atomically dispersed M–N sites in these catalysts. We optimized the synthesis and oxidase-like activity test conditions of FeN_5 SA/CNF (figs. S16

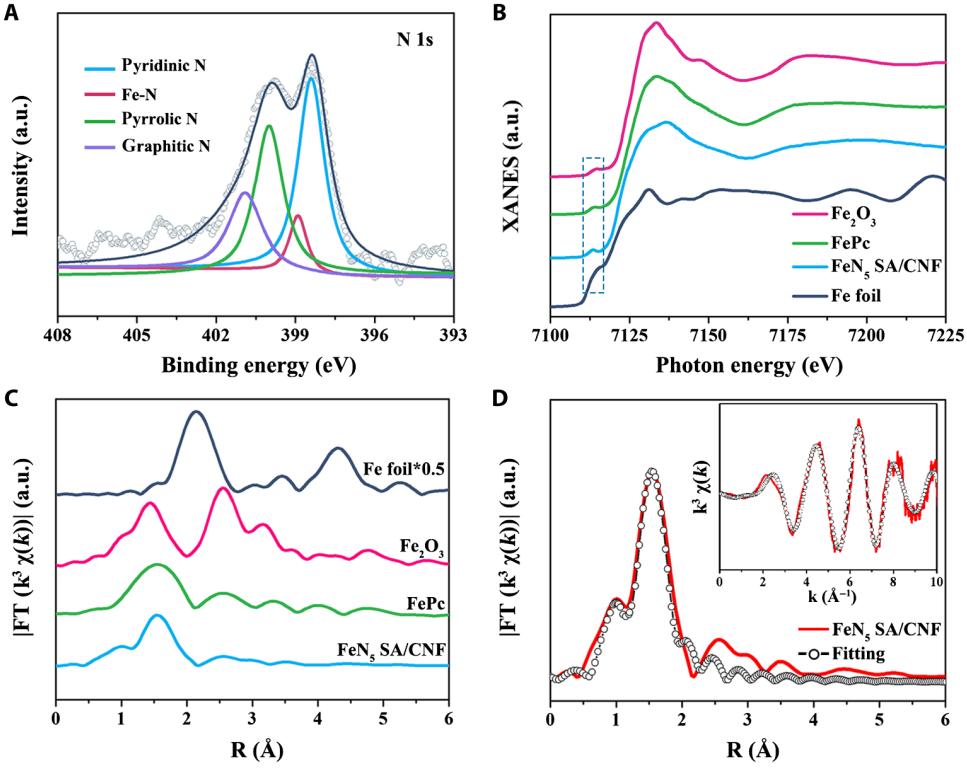

Fig. 2. Atomic structure characterization of FeN_5SA/CNF. (**A**) XPS spectrum of N 1s. a.u., arbitrary unit. (**B**) Normalized XANES spectra at Fe K-edge of the Fe foil, Fe_2O_3, FePc, and FeN_5 SA/CNF and (**C**) the corresponding k^3-weighted Fourier-transformed spectra. (**D**) Fitting curves of the EXAFS of FeN_5 SA/CNF in the r-space and k-space [inset of (D)].

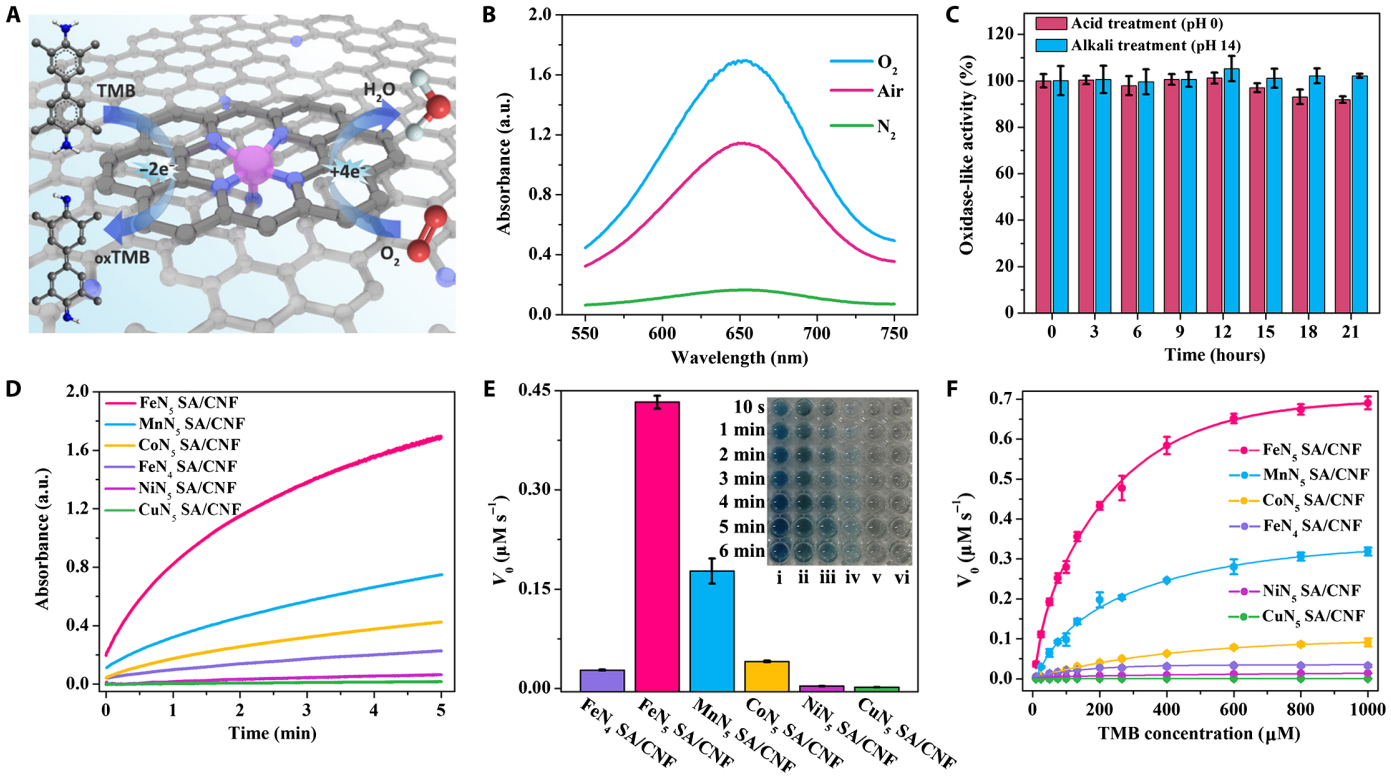

Fig. 3. Oxidase-like activity of FeN_5SA/CNF. (**A**) Schematic illustration of oxidase-like characteristics of FeN_5 SA/CNF–catalyzed TMB oxidation. (**B**) Ultraviolet-visible (UV-vis) absorption spectra of FeN_5 SA/CNF in O_2-saturated, air-saturated, and N_2-saturated sodium acetate–acetic acid buffer. (**C**) The durability of FeN_5 SA/CNF treated with acid (alkali) for 21 hours. (**D**) Time-dependent absorbance changes at 652 nm, (**E**) histogram of V_0, and (**F**) typical Michaelis-Menten curves in the presence of FeN_5 SA/CNF (i), MnN_5 SA/CNF (ii), CoN_5 SA/CNF (iii), FeN_4 SA/CNF (iv), NiN_5 SA/CNF (v), and CuN_5 SA/CNF (vi) in air-saturated sodium acetate–acetic acid buffer. The inset of (E) is an optical image of the TMB solution catalyzed by corresponding catalysts. Photo credit: Liang Huang, Changchun Institute of Applied Chemistry.

and S17). The oxidase-like activities of FeN_5 SA/CNF are highly dependent on the pyrolysis temperature. After pyrolyzing of the FePc@Zn-MOF precursor at 900°C, the optimum reconstitution of carbon nanoframes and FeN_5 active centers leads to a catalytic structure similar to oxidase and active sites more efficient and accessible to substrates. Thus, the FeN_5 SA/CNF exhibits higher oxidase-like activity than other FeN_x SA/CNF and FePc. In addition, the FeN_5 SA/CNF can still retain at least 80 and 90% of the oxidase-like activity even when the test temperature is extended to 60°C and the catalysts undergo 21 hours of strong acid (alkali) treatment, respectively (Fig. 3C and fig. S17A). Compared to the time-dependent absorbance at 652 nm of FeN_5 SA/CNF in air-saturated buffer, the reaction rates of FeN_5 SA/CNF–catalyzed TMB oxidation show a significant increase in O_2-saturated conditions and a sharp decrease in N_2-saturated conditions. These suggest the intense catalytic action of FeN_5 SA/CNF in catalyzing O_2 reduction and that the oxidation rate of TMB is highly dependent on O_2 concentration (Fig. 3B and fig. S18).

Then, we systematically studied the oxidase-like activities of FeN_4 SA/CNF and MN_5 SA/CNF where (M is Mn, Fe, Co, Ni, and Cu). As shown in Fig. 3D, the absorbance of oxidized TMB (oxTMB) immediately reaches 1.0 arbitrary unit (a.u.) in 1 min with the catalysis of FeN_5 SA/CNF, which is much higher than that of other catalysts. As a result, distinct color change is well observed in solution; the colorless TMB can be transformed into blue oxTMB with different catalysts over time. The initial reaction rates of TMB oxidation are calculated by normalizing the absorbance, and FeN_5 SA/CNF exhibit the highest oxidase-like activity of 0.44 μM s^{-1}, which is 17 times higher than that of the FeN_4 SA/CNF (Fig. 3E). Furthermore, the experimental order of oxidase-like activity is FeN_5 SA/CNF > MnN_5 SA/CNF > CoN_5 SA/CNF > FeN_4 SA/CNF ≫ NiN_5 SA/CNF > CuN_5 SA/CNF, indicating that the central metal atom and axial five-N–coordinated structure are of equal importance for single-atom nanozymes. The synergistic effects of these factors give rise to the superior oxidase-like characteristics of FeN_5 SA/CNF. In addition, compared with most reported nanoparticles with oxidase-like characteristics, such as CeO_2, Fe_3O_4, MnO_2, CuO, Au, Pd, Pt, and prussian blue, FeN_5 SA/CNF exhibits oxidase-like activity that outperforms these nanozymes even with merely 1.2 wt % Fe content (fig. S19 and table S2); in particular, the catalytic rate constant (k_{cat}) of FeN_5 SA/CNF is 70 times greater than that of the commercial Pt/C (table S3). Moreover, to the best of our knowledge, the single-atom nanozymes of FeN_5 SA/CNF exhibit more than 30 to 1000 times greater oxidase-like catalytic rate constant than other conventional nanozymes (table S6). These indicate that the superior oxidase-like activities of Fe atoms are derived from the highly dispersed atomic sites and the intrinsic coordination structure. The inhibitive effect of TMB oxidation reaction by ascorbic acid (AA) makes the FeN_5 SA/CNF sensitive to the antioxidant. The oxidation rate of TMB gradually decreases with the increase of AA concentration, and there is a good linear relationship between the absorbance of oxTMB and AA concentration in the range of 0.1 to 10 μM with a limit of detection of 0.07 μM (fig. S20). In view of the high-oxidation catalytic activity and unique catalytic

pathway of oxidase-like characteristics, the single-atom nanozymes of FeN_5 SA/CNF would generate reactive oxygen species or oxidative stress during the catalytic reduction of oxygen, which were able to seriously impair the membrane integrity of bacteria and enhance antibacterial efficiency (*31*–*33*). To accurately evaluate the antibacterial activity of FeN_5 SA/CNF, we used in vitro antibacterial experiments. In comparison to the control group, the bacterial survival rates of *Escherichia coli* and *Staphylococcus aureus* cells exposed to FeN_5 SA/CNF were markedly reduced, indicating that the high oxidase-like activities of FeN_5 SA/CNF could significantly enhance the antibacterial activity. The fluorescence-based live-dead cell assays showed that most of the bacteria emitted red fluorescence with the staining of propidium iodide (PI) after incubating with FeN_5 SA/CNF, suggesting the occurrence of significant membrane damage. Furthermore, the destruction of the cell membrane in SEM images was in accord with the fluorescence assays, bacteria were severely damaged with loss of cell morphology, and extensive membrane damage resulted in the cell collapse (fig. S21). In addition, we conducted cytotoxicity experiments through comparing the effects of FeN_5 SA/CNF on the viability of normal colon mucosa (NCM460) cells. As a result, no obvious toxicity was observed in cell lines, even at the high concentration of FeN_5 SA/CNF (500 μg ml^{-1}) (fig. S22). We used in vivo antibacterial experiments of the actual wound infection model on Balb/c mice to assess the practical antibacterial efficacy of FeN_5 SA/CNF. As shown in fig. S23, within the 4-day observation of the wound after *E. coli* infection and therapy, we observed the clear remission of ulceration and accelerated wound healing in the mice treated with FeN_5 SA/CNF compared to the control group, which coincided with the hematoxylin and eosin (H&E) staining of infected wounds. The staining results indicated that the keratinocytes migrated to the wound site from the normal tissue, and the epidermis gradually became complete and thick in the normal skin sections after treatment (*34*, *35*). Overall, these results indicated that the synthesized FeN_5 SA/CNF were highly biocompatible bactericidal nanozymes.

Further research into the catalytic mechanism on FeN_5 SA/CNF was carried out by steady-state kinetic assay and electron paramagnetic resonance (EPR) analysis. We used typical Michaelis-Menten curves conducted by altering the concentration of TMB for calculating the Michaelis constant (K_m) through the Lineweaver-Burk equation (table S3). The low K_m value of FeN_5 SA/CNF reveals the ultrahigh affinity of FeN_5 active centers toward TMB (Fig. 3F and fig. S24), and the highest k_{cat}/K_m value for FeN_5 SA/CNF indicates the much higher catalytic efficiency than other catalysts (*36*). Besides, high-valent Fe(IV)=O intermediate (compounds I or II iron) is suggested to be a plausible and essential active transient state in catalytic cycles of heme-containing enzymes, which generally exist in heme analogs as well (*27*). To verify whether the FeN_5 active site of FeN_5 SA/CNF generates an Fe(IV)=O intermediate as is seen in heme, we conducted EPR spectroscopy through the reaction of FeN_5 SA/CNF with excess phenyloxoiodine (PhIO) at 77 K. A typical rhombic marker signal at $g \approx 2.03$, consistent with η^2-peroxo heme species, indicates the formation of the Fe(IV)=O intermediate and the similar reaction process with oxidase (fig. S25A). The oxidase-like activity of FeN_5 SA/CNF rapidly decreases against the addition of excess KSCN for the strong coordination of SCN^- with FeN_5 moieties and the poisoning of FeN_5 SA/CNF. This demonstrates that atomically dispersed FeN_5 sites are actual active centers in these catalysts as well (fig. S25B).

Theoretical evaluation on oxidase-like activity

To elucidate the origin of the enhanced oxidase-like activity of FeN_5 SA/CNF, we performed density functional theory (DFT) calculations for the oxygen molecular reduction process on single-atom metal sites with TMB molecules as the reducing agent in acidic conditions (*19*, *27*). The result is represented in terms of the change of free energy on the basis of the proposed four-electron pathway (Fig. 4A and fig. S26B). First, we build an FeN_4 structure in a graphene matrix coupled with pyridinic N as the optimized calculation model of FeN_5 SA/CNF (fig. S26A). In view of the negligible oxidase-like activity and infeasible transition state of NiN_5 SA/CNF and CuN_5 SA/CNF, here, we investigated the active oxidase-like catalysts of FeN_4 SA/CNF, MnN_5 SA/CNF, FeN_5 SA/CNF, and CoN_5 SA/CNF. The first step of O_2 adsorption determines the following activity of electron transfer from active centers to adsorbed intermediates. The calculated adsorption energy (ΔG_{*O2}) suggests the different adsorption strength of O_2 on the adsorption configuration of these catalysts (Fig. 4B, fig. S25C, and table S4 and S5). For the highest ΔG_{*O2}, the O—O distance of adsorbed $*O_2$ on FeN_5 SA/CNF is much larger than that of free molecular O_2 (1.23 Å). This indicates that the strong

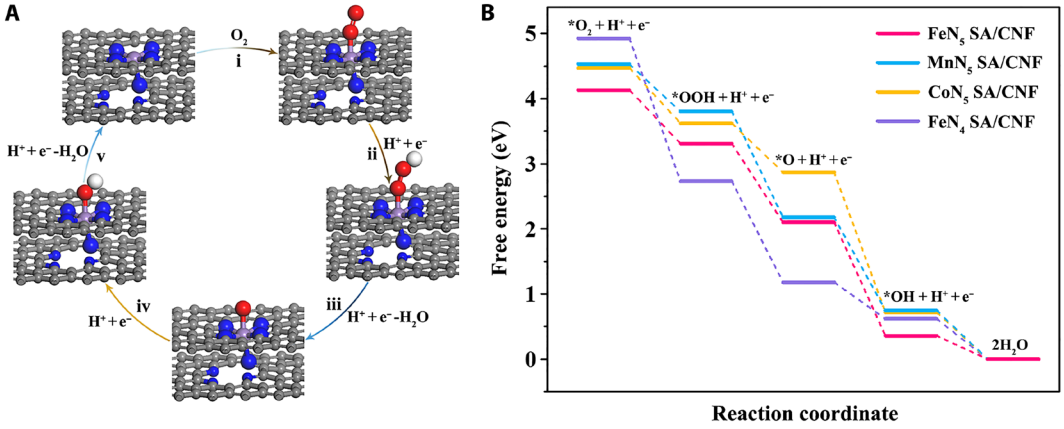

Fig. 4. Theoretical investigation of oxidase-like activity over FeN_5SA/CNF. (**A**) Proposed reaction pathways of O_2 reduction to H_2O with optimized adsorption configurations on FeN_5 SA/CNF. The gray, blue, purple, red, and white balls represent the C, N, Fe, O, and H atoms, respectively. (**B**) Free energy diagram for oxygen reduction reaction on single-atom enzyme mimics with TMB as reductant in an acidic medium.

adsorption weakens the O—O bond and gives rise to a larger extent of O—O bond elongation. The weakening of the O—O bond can be ascribed to the filling of the antibonding π* orbital of O_2 by electrons transferred via the electron push effect of axial-coordinated N in FeN_5 SA/CNF during adsorption (*37*). This behavior looks similar to that of the strong internal electron donor from axial thiolate ligand of cytochrome P450 (*38*, *39*). On the other hand, the ultralow ΔG_{*O2} (0.05 eV) of the square planar FeN_4 SA/CNF leads to the weak adsorption of O_2 and activation of the O—O bond, thereby restricting the reaction rate and oxidase-like activity. In addition, MnN_5 SA/CNF and CoN_5 SA/CNF have moderate ΔG_{*O2}, but the higher G_{*O} of CoN_5 SA/CNF results in the high-energy barrier of the third step ($*OOH + H^+ + e^- \rightarrow *O + H_2O$), thus MnN_5 SA/CNF are better able to cleave the O—O bond of adsorbed *OOH than CoN_5 SA/CNF is. According to these energetics, the calculated order of oxidase-like activity is FeN_5 SA/CNF > MnN_5 SA/CNF > CoN_5 SA/CNF > FeN_4 SA/CNF, coinciding with the experimental results. To sum up, compared with the square planar FeN_4 SA/CNF, the additional axial-coordinated N atom gives FeN_5 SA/CNF a strong electron push effect, which activates O_2 and favors the cleavage of the O—O bond, thus promoting the oxidative capability of the Brønsted-basic adsorbed oxo species toward acquiring acidic hydrogens from substrates (TMB) en route to the oxidation of the substrates (*19*, *26*, *27*). Meanwhile, the synergistic effects between the central metal Fe atom and axial N-coordinated structure effectively optimize the free energy of each transition state on FeN_5 SA/CNF under moderate conditions. Therefore, the DFT calculations unambiguously identify that the central metal atom and the steric configuration of single-atom nanozymes are the origin of superior oxidase-like activity.

DISCUSSION

In summary, we have discovered a new class of single-atom nanozymes with atomically dispersed enzyme-like active sites in nanomaterials. The maximized atomic utilization efficiency and well-defined active moieties significantly enhanced the catalytic performance relative to conventional nanozymes and uncovered the underlying mechanism. With oxidase catalysis as a model reaction, both experimental studies and theoretical calculations revealed that the synthesized single-atom nanozymes of FeN_5 SA/CNF catalytically behaved like the axial-coordinated hemes of oxidoreductases. The electron push-effect mechanism and crucial synergistic effects endow FeN_5 SA/CNF with the highest oxidase-like activity among other nanozymes; in particular, the catalytic rate constant of FeN_5 SA/CNF is 70 times greater than that of the commercial Pt/C. Meanwhile, FeN_5 SA/CNF exhibited broad-spectrum bactericidal properties in vitro and efficient wound disinfection in vivo. The present results suggest that the defined single-atom nanozymes provide a new perspective to the catalytic mechanism and rational design of nanozymes and exhibit great potential to become the next-generation nanozymes.

MATERIALS AND METHODS

Materials

2,2′-Bipyridine-5,5′-dicarboxylic acid (H_2bpydc, >97%) was purchased from Ark Pharm Inc. 1,1′-Biphenyl-4,4′-dicarboxylic acid (H_2bpdc, 97%), lauric acid (LA, 98%), *N*,*N*-dimethylacetamide (DMAC, 98%), zinc acetate dihydrate [$Zn(OAc)_2$, 98%], and polyvinyl pyrrolidone (PVP K-30, 99%) were purchased from Sigma-Aldrich. Manganese(II) phthalocyanine (MnPc, 97%) and nickel(II) phthalocyanine (NiPc, 97%) were purchased from Alfa Aesar. FePc (97%), cobalt(II) phthalocyanine (CoPc, 95%), copper(II) phthalocyanine (CuPc, 99%) and TMB (98%) were purchased from Aladdin (Shanghai, China). All chemicals were used as received without any further purification.

Methods

Synthesis of FeN_5 SA/CNF

The FePc@MOF precursor was prepared via a one-step hydrothermal synthesis with FePc molecules in situ encapsulating in $[Zn(bpydc)(DMAC)]_n$. In a typical synthesis, 50 mg of H_2bpdc, 20 mg of PVP, 20 mg of LA, and 2 mg of FePc were dissolved in 20 ml of DMAC, followed by sonication and vigorous stirring for 2 hours, and then 150 mg of $Zn(OAc)_2$ was added to the solution with stirring for an additional 1 min. The mixed solution was transferred into a 40-ml Teflon-lined high-pressure vessel and heated at 100°C for 12 hours in an electric oven before it was cooled to room temperature. The product was collected by centrifugation and washed several times with DMAC-ethanol solution. After drying in a vacuum oven, the precursor was placed in the center of a quartz tube furnace and annealed at 900°C for 2 hours under of N_2 flow to obtain FeN_5 SA/CNF. The synthesis of CoN_5 SA/CNF, NiN_5 SA/CNF, CuN_5 SA/CNF, and MnN_5 SA/CNF was similar to that of FeN_5 SA/CNF, except that FePc was replaced by equal moles of the corresponding MPc. FeN_4 SA/CNF was synthesized by simply replacing H_2bpydc with H_2bpdc and without using PVP while keeping the other reaction parameters the same. The as-obtained product was treated with 0.1 M HCl for 2 hours to remove unvolatile zinc and then washed several times with deionized water and dried for further characterization.

Instrumentation

TEM images were characterized by a JEM-2010 operating at 200 kV. SEM images were measured with an XL30 ESEM FEG SEM (Philips, Netherlands) operating with an accelerating voltage of 20 kV. The atomic-resolution HAADF-STEM images were obtained by using a Titan 80-300 STEM operated at 300 kV, equipped with a probe spherical aberration corrector. XRD patterns were collected on a D8 ADVANCE (Bruker AXS, Germany) diffractometer using Cu Kα radiation. XPS measurements were conducted on an ESCALAB MKII spectrometer (VG Co., UK) with Al Kα x-ray radiation as the x-ray source for excitation. The nitrogen adsorption/desorption isotherms were obtained with an ASAP 2020 Physisorption Analyzer (Micrometrics Instrument Corporation). The metal loadings of the catalysts were measured by ICP-MS, which were obtained by a Thermo Scientific iCAP6300 (Thermo Fisher Scientific, USA). X-band EPR spectroscopy was conducted on a Bruker spectrometer equipped with an Oxford ESR-910 liquid helium cryostat. The microwave frequency was calibrated with a frequency counter and the magnetic field with a nuclear magnetic resonance gauss meter. Typical experimental parameters were as follows: 77 K, 9.853 GHz, a microwave power of 10.8 mW, a modulation of 100 kHz, and a modulation amplitude of 10 G. XAFS spectra operated at 2.5 GeV with a maximum current of 250 mA were obtained at the 1W1B station at the Beijing Synchrotron Radiation Facility (P. R. China). XAFS measurements at the Fe, Co, Ni, Cu, and Mn K-edges were performed in fluorescence mode using a Lytle detector. All samples were tabletized as disks with a diameter of 13 mm and a thickness of 1.0 mm using graphite powder as binder. The acquired EXAFS data were processed according to the

standard procedures using the ATHENA module implemented in the IFEFFIT software packages. The EXAFS spectra were obtained by subtracting the post-edge background from the overall absorption and then normalizing with respect to the edge jump step. Then, $\chi(k)$ data in the k-space ranging from 2.6 to 12.6 $Å^{-1}$ were Fourier-transformed to real (R) space using hanning windows (d_k = 1.0 $Å^{-1}$) to separate the EXAFS contributions from different coordination shells. The ^{57}Fe Mössbauer spectrum was carried out on a Topologic 500A spectrometer driving with a proportional counter at room temperature. The radioactive source was ^{57}Co (Rh) moving in a constant acceleration mode. Data analyses were performed assuming a Lorentzian line shape for computer folding and fitting. The components of iron phases were identified based on their Mössbauer parameters including δ_{iso}, ΔE_Q, magnetic hyperfine field, and relative area of Fe ions.

Oxidase-like activity

Oxidase activities were determined by colorimetric assays. Ten microliters of catalysts (0.5 mg ml^{-1}) and 20 μl of 20 mM TMB were added into a 1.5-ml tube containing 970 μl of sodium acetate–acetic acid buffer [100 mM (pH 4.0)]. The catalytic oxidation of TMB (oxTMB) was studied by measuring the absorption changes of the oxidized form of TMB at λ_{max} = 652 nm (ε = 39,000 $M^{-1}\cdot cm^{-1}$). Unless otherwise stated, oxidase activities were carried out in air-saturated buffer. To explore the optimal conditions of the oxidation of TMB with single-atom nanozymes, a range of temperatures (20° to 60°C) and pH values (2.0 to 9.0) for the reaction were measured under the same conditions mentioned above. The Michaelis-Menten constant was calculated using Lineweaver-Burk plots of the double reciprocal of the Michaelis-Menten equation $v = v_{max} \times [S]/(K_m + [S])$, where v is the initial velocity, v_{max} is the maximal reaction velocity, [S] is the concentration of substrate, and K_m is the Michaelis constant. The catalytic rate constant (k_{cat}) defined as $k_{cat} = v_{max}/[E]$ was calculated, where [E] is the molar concentration of metal in single-atom nanozymes.

Colorimetric detection of AA

Ten microliters of FeN_5 SA/CNF (0.5 mg ml^{-1}) were added into a 1.5-ml tube containing 970 μl of sodium acetate–acetic acid buffer [100 mM (pH 4.0)]. Then, 20 μl of 20 mM TMB with varying concentrations of AA (0.1 to 50 μM) was added into the solution. The catalytic oxidation of substrates was studied by measuring the absorption changes of the oxTMB at λ_{max} = 652 nm (ε = 39,000 $M^{-1}\cdot cm^{-1}$). The colorimetric detection of AA was carried out in air-saturated buffer.

Bacterial culture and antibacterial experiments

Monocolonies of *E. coli* and *S. aureus* on the solid Luria-Bertani (LB) agar plates were transferred to 20 ml of liquid LB broth [yeast extract, 5 g $liter^{-1}$; tryptone, 10 g $liter^{-1}$; and NaCl, 5 g $liter^{-1}$ (pH 7.0)] and grown at 37°C for 12 hours at a rotation of 200 rpm. Then, the bacteria were diluted with phosphate-buffered saline (PBS) solution [10 mM (pH 5.5)] to 10^7 colony-forming units (CFU) ml^{-1} and mixed with FeN_5 SA/CNF (100 μg ml^{-1}) for 40 min. Both *E. coli* and *S. aureus* bacteria were stained with PI (10 μg ml^{-1}) for 15 min in the dark and washed twice with PBS. The membrane-impermeant PI would only enter through damaged bacteria membranes; thus, it was used to label dead bacteria with red fluorescence. The live and dead bacterial cells were then visualized with a fluorescence microscope. The concentration of bacteria was monitored spectrophotometrically by measuring the optical density at 600 nm (OD_{600}).

Morphology observation of bacteria

After the antibacterial assessment, four typical groups of the bacterial suspensions were dropped on silicon wafers and fixed with 2% glutaraldehyde-containing PBS solution for 4 hours at 4°C. Then, the bacteria were dehydrated by sequential treatments with 30, 50, 70, 90, and 100% of ethanol for 10 min, respectively. Dried bacteria were sputter-coated with gold for field-emission SEM images.

In vitro cytotoxicity experiments

NCM460 cells were used for the investigation of the cell viabilities. NCM460 cells were grown in normal Dulbecco's modified Eagle's medium with 10% fetal bovine serum. The in vitro cytotoxicity was measured by a standard Cell Counting Kit-8 (CCK-8) assay. The cells were incubated in a 96-well plate (about 5000 cells per well, eight wells for each concentration) for 24 hours in a humidified incubator (37°C, 5% CO_2), then each well was washed with PBS (10 mM, pH 7.4), and FeN_5 SA/CNF in different concentrations (0, 100, 200, 300, 400, and 500 μg ml^{-1}) were added. Then, the cells were coincubated for 24 hours. CCK-8 was subsequently added to each well, and the plate was kept in the incubator for another 1.5 hours. Last, cell viability was evaluated by the absorbance at 450 nm of each well by a microplate reader (SpectraMax M2, MDC, USA). Cells without FeN_5 SA/CNF were used as control, and the culture medium without cells but with CCK-8 were considered as background. Cell viability was calculated relative to the control cells.

In vivo mice wound model

To evaluate the antibacterial effects of FeN_5 SA/CNF in vivo, the injury model was built. Female Balb/c mice (6 to 8 weeks and 17 to 21 g) were randomly divided into two groups (five mice per group). A wound about 16 mm^2 was obtained by surgical procedure on the back of each mouse after anesthesia. The wounds were then infected by 20 μl of *E. coli* bacterial suspension (1×10^7 CFU ml^{-1}). After 12 hours, 10 μl of FeN_5 SA/CNF (100 μg ml^{-1}) and PBS solutions were dropped on the wound area at the corresponding groups. The wounds of infection were recorded and photographed within 4 days. After 4 days, the wound tissues were harvested from the mice for analysis after euthanasia. To determine the amount of bacteria, the wound tissues were placed in 1 ml of PBS and homogenized, and then, the solutions were cultured in liquid LB broth at 37°C for 24 hours at a rotation of 200 rpm before measuring the OD_{600}. Animal studies were conducted in compliance with the guidelines of the Institutional Animal Care and Use Committee. The mice were discarded according to the standard approved protocol after we finished the experiment.

Histological analysis

The wound tissues in different groups were fixed in neutral buffered formalin, processed routinely into paraffin, sectioned into about 4-μm slices, and stained with H&E. The samples were examined under a digital microscope.

Computational studies

The spin-unrestricted calculations in this study were performed with the package DMol^3 in Materials Studio 17.1 at the DFT level (*40*, *41*). The generalized gradient-corrected Perdew-Burke-Ernzerhof functional (*42*), along with a double numerical basis set including p-polarization function, was applied for all calculations. The core treatment of MN_5C (M = Fe, Co, and Ni) and FeN_4C is the density functional semicore pseudopotential, which includes some degree of relativistic correction. A dispersion-corrected DFT scheme was used to describe the van der Waals interaction. The solution

effect of water was accounted by using the conductor-like screening model. During the coordinates relaxation, the tolerances of energy and force were 1×10^{-5} Ha and 0.002 Ha/Å, respectively, and the maximum displacement was 5×10^{-3} Å. The Monkhorst-Pack *k*-point mesh was set to be $4 \times 4 \times 1$, and the global orbital cutoff was set as 5.0 Å after a convergence test. The free energies of the reactions at 298.15 K were calculated with the partial hessian vibrational analysis method (*43*). The equations of O_2 reduction with four-electron pathway in the free energy profiles calculation are as follows:

(i) $*O_2 + H^+ + e^- = *OOH$

(ii) $*OOH + H^+ + e^- = *O + H_2O$

(iii) $*O + H^+ + e^- = *OH$

(iv) $*OH + H^+ + e^- = * + H_2O$

The asterisk (*) indicates the adsorption sites on a metal surface. The free energy was calculated by the equation $G = E + ZPE - TS$, where E is the total energy, ZPE is the zero-point energy, T is the temperature in kelvin, and S is the entropy.

SUPPLEMENTARY MATERIALS

Supplementary material for this article is available at http://advances.sciencemag.org/cgi/content/full/5/5/eaav5490/DC1

Fig. S1. The structures of cytocrome P450, horseradish peroxidase, and catalase and the corresponding active center.
Fig. S2. Morphology of the Zn-MOF precursor.
Fig. S3. Structure of the Zn-MOF precursor.
Fig. S4. FTIR spectra of FePc, Zn-MOF, and FePc@Zn-MOF.
Fig. S5. Morphology and structure of FeN_5 SA/CNF.
Fig. S6. Surface area and pore structure characterization.
Fig. S7. HRTEM images of FeN_5 SA/CNF.
Fig. S8. XPS and Mössbauer spectra of FeN_5 SA/CNF.
Fig. S9. Morphology and atomic structure of FeN_5 SA/CNF@800°C.
Fig. S10. Morphology and atomic structure of FeN_5 SA/CNF@1000°C.
Fig. S11. Morphology and atomic structure of FeN_4 SA/CNF.
Fig. S12. Morphology and atomic structure of MnN_5 SA/CNF.
Fig. S13. Morphology and atomic structure of CoN_5 SA/CNF.
Fig. S14. Morphology and atomic structure of NiN_5 SA/CNF.
Fig. S15. Morphology and atomic structure of CuN_5 SA/CNF.
Fig. S16. UV-vis absorption spectra of the catalysts.
Fig. S17. Oxidase-like activities of FeN_5 SA/CNF in different conditions.
Fig. S18. UV-vis absorption spectra of FeN_5 SA/CNF.
Fig. S19. Morphology and structure of synthesized conventional nanozymes.
Fig. S20. UV-vis absorption spectra of TMB solutions.
Fig. S21. Morphological changes in bacteria.
Fig. S22. In vitro cytotoxicity experiments.
Fig. S23. Photographs of in vivo mice wound model.
Fig. S24. Double-reciprocal plots of activity of these catalysts.
Fig. S25. The analysis of the intermediate state of and active center in FeN_5 SA/CNF.
Fig. S26. Theoretical investigation of oxidase-like activity.
Table S1. Mössbauer parameters of FeN_5 SA/CNF.
Table S2. Comparison of oxidase-like activity of synthesized catalysts.
Table S3. Comparison of the kinetic constants of the single-atom enzyme mimics.
Table S4. The adsorption energy on the single-atom catalysts.
Table S5. Reaction free energy of intermediate species on single-atom catalysts.
Table S6. Comparison of the kinetic constants of FeN_5 SA/CNF and nanozymes.
References (*44*–*51*)

REFERENCES AND NOTES

1. H. Wei, E. Wang, Nanomaterials with enzyme-like characteristics (nanozymes): Next-generation artificial enzymes. *Chem. Soc. Rev.* **42**, 6060–6093 (2013).
2. J. Wu, X. Wang, Q. Wang, Z. Lou, S. Li, Y. Zhu, L. Qin, H. Wei, Nanomaterials with enzyme-like characteristics (nanozymes): Next-generation artificial enzymes (II). *Chem. Soc. Rev.* **48**, 1004–1076 (2019).
3. N. A. Kotov, Inorganic nanoparticles as protein mimics. *Science* **330**, 188–189 (2010).
4. X. Wang, Y. Hu, H. Wei, Nanozymes in bionanotechnology: From sensing to therapeutics and beyond. *Inorg. Chem. Front.* **3**, 41–60 (2016).
5. L. Gao, J. Zhuang, L. Nie, J. Zhang, Y. Zhang, N. Gu, T. Wang, J. Feng, D. Yang, S. Perrett, X. Yan, Intrinsic peroxidase-like activity of ferromagnetic nanoparticles. *Nat. Nanotechnol.* **2**, 577–583 (2007).
6. F. Natalio, R. André, A. F. Hartog, B. Stoll, K. P. Jochum, R. Wever, W. Tremel, Vanadium pentoxide nanoparticles mimic vanadium haloperoxidases and thwart biofilm formation. *Nat. Nanotechnol.* **7**, 530–535 (2012).
7. K. Fan, J. Xi, L. Fan, P. Wang, C. Zhu, Y. Tang, X. Xu, M. Liang, B. Jiang, X. Yan, L. Gao, In vivo guiding nitrogen-doped carbon nanozyme for tumor catalytic therapy. *Nat. Commun.* **9**, 1440 (2018).
8. Q. Wang, X. Zhang, L. Huang, Z. Zhang, S. Dong, GOx@ZIF-8(NiPd) nanoflower: An artificial enzyme system for tandem catalysis. *Angew. Chem. Int. Ed.* **56**, 16082–16085 (2017).
9. A. Asati, S. Santra, C. Kaittanis, S. Nath, J. M. Perez, Oxidase-like activity of polymer-coated cerium oxide nanoparticles. *Angew. Chem. Int. Ed.* **48**, 2308–2312 (2009).
10. I. Nath, J. Chakraborty, F. Verpoort, Metal organic frameworks mimicking natural enzymes: A structural and functional analogy. *Chem. Soc. Rev.* **45**, 4127–4170 (2016).
11. S. Hou, X. Hu, T. Wen, W. Liu, X. Wu, Core-shell noble metal nanostructures templated by gold nanorods. *Adv. Mater.* **25**, 3857–3862 (2013).
12. D. Pedone, M. Moglianetti, E. De Luca, G. Bardi, P. P. Pompa, Platinum nanoparticles in nanobiomedicine. *Chem. Soc. Rev.* **46**, 4951–4975 (2017).
13. M. Liang, K. Fan, Y. Pan, H. Jiang, F. Wang, D. Yang, D. Lu, J. Feng, J. Zhao, L. Yang, X. Yan, Fe_3O_4 magnetic nanoparticle peroxidase mimetic-based colorimetric assay for the rapid detection of organophosphorus pesticide and nerve agent. *Anal. Chem.* **85**, 308–312 (2013).
14. M. Kluenker, M. Nawaz Tahir, R. Ragg, K. Korschelt, P. Simon, T. E. Gorelik, B. Barton, S. I. Shylin, M. Panthöfer, J. Herzberger, H. Frey, V. Ksenofontov, A. Möller, U. Kolb, J. Grin, W. Tremel, Pd@Fe_2O_3 superparticles with enhanced peroxidase activity by solution phase epitaxial growth. *Chem. Mater.* **29**, 1134–1146 (2017).
15. Y. Liu, D. L. Purich, C. Wu, Y. Wu, T. Chen, C. Cui, L. Zhang, S. Cansiz, W. Hou, Y. Wang, S. Yang, W. Tan, Ionic functionalization of hydrophobic colloidal nanoparticles to form ionic nanoparticles with enzymelike properties. *J. Am. Chem. Soc.* **137**, 14952–14958 (2015).
16. B. Reuillard, S. Gentil, M. Carrière, A. Le Goff, S. Cosnier, Biomimetic versus enzymatic high-potential electrocatalytic reduction of hydrogen peroxide on a functionalized carbon nanotube electrode. *Chem. Sci.* **6**, 5139–5143 (2015).
17. Y. Lin, J. Ren, X. Qu, Catalytically active nanomaterials: A promising candidate for artificial enzymes. *Acc. Chem. Res.* **47**, 1097–1105 (2014).
18. Q. Q. Wang, H. Wei, Z. Zhang, E. Wang, S. Dong, Nanozyme: An emerging alternative to natural enzyme for biosensing and immunoassay. *TrAC Trends Anal. Chem.* **105**, 218–224 (2018).
19. X. Shen, W. Liu, X. Gao, Z. Lu, X. Wu, X. Gao, Mechanisms of oxidase and superoxide dismutation-like activities of gold, silver, platinum, and palladium, and their alloys: A general way to the activation of molecular oxygen. *J. Am. Chem. Soc.* **137**, 15882–15891 (2015).
20. S. Ghosh, P. Roy, N. Karmodak, E. D. Jemmis, G. Mugesh, Nanoisozymes: Crystal-facet-dependent enzyme-mimetic activity of V_2O_5 nanomaterials. *Angew. Chem. Int. Ed.* **57**, 4510–4515 (2018).
21. M. D. Marcinkowski, M. T. Darby, J. Liu, J. M. Wimble, F. R. Lucci, S. Lee, A. Michaelides, M. Flytzani-Stephanopoulos, M. Stamatakis, E. C. H. Sykes, Pt/Cu single-atom alloys as coke-resistant catalysts for efficient C-H activation. *Nat. Chem.* **10**, 325–332 (2018).
22. B. Qiao, A. Wang, X. Yang, L. F. Allard, Z. Jiang, Y. Cui, J. Liu, J. Li, T. Zhang, Single-atom catalysis of CO oxidation using Pt1/FeOx. *Nat. Chem.* **3**, 634–641 (2011).
23. D. H. Deng, X. Chen, L. Yu, X. Wu, Q. Liu, Y. Liu, H. Yang, H. Tian, Y. Hu, P. Du, R. Si, J. Wang, X. Cui, H. Li, J. Xiao, T. Xu, J. Deng, F. Yang, P. N. Duchesne, P. Zhang, J. Zhou, L. Sun, J. Li, X. Pan, X. Bao, A single iron site confined in a graphene matrix for the catalytic oxidation of benzene at room temperature. *Sci. Adv.* **1**, e1500462 (2015).
24. H. Fei, J. Dong, Y. Feng, C. S. Allen, C. Wan, B. Volosskiy, M. Li, Z. Zhao, Y. Wang, H. Sun, P. An, W. Chen, Z. Guo, C. Lee, D. Chen, I. Shakir, M. Liu, T. Hu, Y. Li, A. I. Kirkland, X. Duan, Y. Huang, General synthesis and definitive structural identification of MN_4C_4 single-atom catalysts with tunable electrocatalytic activities. *Nat. Catal.* **1**, 63–72 (2018).
25. W. Liu, L. Zhang, X. Liu, X. Liu, X. Yang, S. Miao, W. Wang, A. Wang, T. Zhang, Discriminating catalytically active FeN_x species of atomically dispersed Fe-N-C catalyst for selective oxidation of the C-H bond. *J. Am. Chem. Soc.* **139**, 10790–10798 (2017).
26. T. L. Poulos, Heme enzyme structure and function. *Chem. Rev.* **114**, 3919–3962 (2014).
27. X. Huang, J. T. Groves, Oxygen activation and radical transformations in heme proteins and metalloporphyrins. *Chem. Rev.* **118**, 2491–2553 (2017).
28. S. J. Dong, R. Jiang, Research on chemically modified electrodes: Electrocatalytic reduction of dioxygen by iron tetraphenylporphyrin modified glassy carbon electrode with heat treatment. *Ber. Bunsen. Phys. Chem* **91**, 479–484 (1987).
29. Y. Pan, S. Liu, K. Sun, X. Chen, B. Wang, K. Wu, X. Cao, W.-C. Cheong, R. Shen, A. Han, Z. Chen, L. Zheng, J. Luo, Y. Lin, Y. Liu, D. Wang, Q. Peng, Q. Zhang, C. Chen, Y. Li, A bimetallic Zn/Fe polyphthalocyanine-derived single-atom Fe-N_4 catalytic site: A

superior trifunctional catalyst for overall water splitting and Zn-air batteries. *Angew. Chem. Int. Ed.* **130**, 8750–8754 (2018).
30. Y. Han, Y. Wang, R. Xu, W. Chen, L. Zheng, A. Han, Y. Zhu, J. Zhang, H. Zhang, J. Luo, C. Chen, Q. Peng, D. Wang, Y. Li, Electronic structure engineering to boost oxygen reduction activity by controlling the coordination of the central metal. *Energ. Environ. Sci.* **11**, 2348–2352 (2018).
31. W. Yin, J. Yu, F. Lv, L. Yan, L. R. Zheng, Z. Gu, Y. Zhao, Functionalized Nano-MoS_2 with peroxidase catalytic and near-infrared photothermal activities for safe and synergetic wound antibacterial applications. *ACS Nano* **10**, 11000–11011 (2016).
32. S. Liu, T. H. Zeng, M. Hofmann, E. Burcombe, J. Wei, R. Jiang, J. Kong, Y. Chen, Antibacterial activity of graphite, graphite oxide, graphene oxide, and reduced graphene oxide: Membrane and oxidative stress. *ACS Nano* **5**, 6971–6980 (2011).
33. W. He, H. K. Kim, W. G. Wamer, D. Melka, J. H. Callahan, J. J. Yin, Photogenerated charge carriers and reactive oxygen species in ZnO/Au hybrid nanostructures with enhanced photocatalytic and antibacterial activity. *J. Am. Chem. Soc.* **136**, 750–757 (2014).
34. Y. Tao, E. Ju, J. Ren, X. Qu, Bifunctionalized mesoporous silica-supported gold nanoparticles: Intrinsic oxidase and peroxidase catalytic activities for antibacterial applications. *Adv. Mater.* **27**, 1097–1104 (2015).
35. Z. Xu, Z. Xiu, Q. Liu, Y. Huang, D. Li, X. Shen, K. Fan, J. Xi, Y. Gu, Y. Tang, J. Jiang, J. Xu, J. He, X. Gao, Y. Liu, H. Koo, X. Yan, L. Gao, Converting organosulfur compounds to inorganic polysulfides against resistant bacterial infections. *Nat. Commun.* **9**, 3713 (2018).
36. B. Jiang, D. Duan, L. Gao, M. Zhou, K. Fan, Y. Tang, J. Xi, Y. Bi, Z. Tong, G. F. Gao, N. Xie, A. Tang, G. Nie, M. Liang, X. Yan, Standardized assays for determining the catalytic activity and kinetics of peroxidase-like nanozymes. *Nat. Protoc.* **13**, 1506–1520 (2018).
37. E. L. Onderko, A. Silakov, T. H. Yosca, M. T. Green, Characterization of a selenocysteine-ligated P450 compound I reveals direct link between electron donation and reactivity. *Nat. Chem.* **9**, 623–628 (2017).
38. C. M. Krest, A. Silakov, J. Rittle, T. H. Yosca, E. L. Onderko, J. C. Calixto, M. T. Green, Significantly shorter Fe-S bond in cytochrome P450-I is consistent with greater reactivity relative to chloroperoxidase. *Nat. Chem.* **7**, 696–702 (2015).
39. J. H. Dawson, Probing structure-function relations in heme-containing oxygenases and peroxidases. *Science* **240**, 433–439 (1988).
40. B. Delley, An all-electron numerical method for solving the local density functional for polyatomic molecules. *J. Chem. Phys.* **92**, 508–517 (1990).
41. B. Delley, From molecules to solids with the $DMol^3$ approach. *J. Chem. Phys.* **113**, 7756–7764 (2000).
42. J. P. Perdew, K. Burke, M. Ernzerhof, Generalized gradient approximation made simple. *Phys. Rev. Lett.* **77**, 3865–3868 (1996).
43. C. K. Acharya, C. H. Turner, CO oxidation with Pt(111) supported on pure and boron-doped carbon: A DFT investigation. *Surf. Sci.* **602**, 3595–3602 (2008).
44. H. Cheng, S. Lin, F. Muhammad, Y.-W. Lin, H. Wei, Rationally modulate the oxidase-like activity of nanoceria for self-regulated bioassays. *ACS Sens.* **1**, 1336–1343 (2016).
45. R. Dalapati, B. Sakthivel, M. K. Ghosalya, A. Dhakshinamoorthy, S. Biswas, A cerium-based metal–organic framework having inherent oxidase-like activity applicable for colorimetric sensing of biothiols and aerobic oxidation of thiols. *CrstEngComm* **19**, 5915–5925 (2017).
46. X. Zhang, Y. Huang, Evaluation of the antioxidant activity of phenols and tannic acid determination with Mn_3O_4nano-octahedrons as an oxidase mimic. *Anal. Methods* **7**, 8640–8646 (2015).
47. J. Zhao, Y. Xie, W. Yuan, D. Li, S. Liu, B. Zheng, W. Hou, A hierarchical Co–Fe LDH rope-like nanostructure: Facile preparation from hexagonal lyotropic liquid crystals and intrinsic oxidase-like catalytic activity. *J. Mater. Chem. B* **1**, 1263–1269 (2013).
48. Q. Chen, C. Liang, X. Zhang, Y. Huang, High oxidase-mimic activity of Fe nanoparticles embedded in an N-rich porous carbon and their application for sensing of dopamine. *Talanta* **182**, 476–483 (2018).
49. L. Fan, X. Xu, C. Zhu, J. Han, L. Gao, J. Xi, R. Guo, Tumor catalytic-photothermal therapy with yolk-shell gold@carbon nanozymes. *ACS Appl. Mater. Interfaces* **10**, 4502–4511 (2018).
50. G.-J. Cao, X. Jiang, H. Zhang, T. R. Croley, J.-J. Yin, Mimicking horseradish peroxidase and oxidase using ruthenium nanomaterials. *RSC Adv.* **7**, 52210–52217 (2017).
51. L. Guo, L. Mao, K. Huang, H. Liu, Pt–Se nanostructures with oxidase-like activity and their application in a selective colorimetric assay for mercury(II). *J. Mater. Sci.* **52**, 10738–10750 (2017).

Acknowledgments: L.H. thanks Y. Zhao for help with the in vivo experiments. **Funding:** We acknowledge the support from the National Natural Science Foundation of China (nos. 21375123 and 21675151) and the Ministry of Science and Technology of China (nos. 2013-YQ170585 and 2016YFA0203203). **Author contributions:** S.D., J.W., and L.H. designed the study. L.H. performed most of the reactions and structural characterization. J.C. conducted the experiments on the oxidase-like activities of these catalysts. L.H. and L.G. finished the DFT calculations. S.D., J.W., L.H., and J.C. wrote the paper. All the authors contributed to the overall scientific interpretation and edited the manuscript. **Competing interests:** The authors declare that they have no competing interests. **Data and materials availability:** All data needed to evaluate the conclusions in the paper are present in the paper and/or the Supplementary Materials. Additional data related to this paper may be requested from the authors.

Submitted 27 September 2018
Accepted 21 March 2019
Published 3 May 2019
10.1126/sciadv.aav5490

Citation: L. Huang, J. Chen, L. Gan, J. Wang, S. Dong, Single-atom nanozymes. *Sci. Adv.* **5**, eaav5490 (2019).